JACS
JOURNAL OF THE AMERICAN CHEMICAL SOCIETY

Article

pubs.acs.org/JACS

Hairy Uniform Permanently Ligated Hollow Nanoparticles with Precise Dimension Control and Tunable Optical Properties

Yihuang Chen,[†,‡] Di Yang,[§] Young Jun Yoon,[†] Xinchang Pang,[†] Zewei Wang,[†] Jaehan Jung,[†] Yanjie He,[†] Yeu Wei Harn,[†] Ming He,[†] Shuguang Zhang,[†,‡] Guangzhao Zhang,[*,‡] and Zhiqun Lin[*,†]

[†]School of Materials Science and Engineering, Georgia Institute of Technology, Atlanta, Georgia 30332, United States
[‡]Faculty of Materials Science and Engineering, South China University of Technology, Guangzhou 510640, China
[§]College of Science, Minzu University of China, Beijing 100081, China

Supporting Information

ABSTRACT: The ability to tailor the size and shape of nanoparticles (NPs) enables the investigation into the correlation between these parameters and optical, optoelectronic, electrical, magnetic, and catalytic properties. Despite several effective approaches available to synthesize NPs with a hollow interior, it remains challenging to have a general strategy for creating a wide diversity of high-quality hollow NPs with different dimensions and compositions on demand. Herein, we report on a general and robust strategy to in situ crafting of monodisperse hairy hollow noble metal NPs by capitalizing on rationally designed amphiphilic star-like triblock copolymers as nanoreactors. The intermediate blocks of star-like triblock copolymers can associate with metal precursors via strong interaction (i.e., direct coordination or electrostatic interaction), followed by reduction to yield hollow noble metal NPs. Notably, the outer blocks of star-like triblock copolymers function as ligands that intimately and permanently passivate the surface of hollow noble metal NPs (i.e., forming hairy permanently ligated hollow NPs with superior solubility in nonpolar solvents). More importantly, the diameter of the hollow interior and the thickness of the shell of NPs can be readily controlled. As such, the dimension-dependent optical properties of hollow NPs are scrutinized by combining experimental studies and theoretical modeling. The dye encapsulation/release studies indicated that hollow NPs may be utilized as attractive guest molecule nanocarriers. As the diversity of precursors are amenable to this star-like triblock copolymer nanoreactor strategy, it can conceptually be extended to produce a rich variety of hairy hollow NPs with different dimensions and functionalities for applications in catalysis, water purification, optical devices, lightweight fillers, and energy conversion and storage.

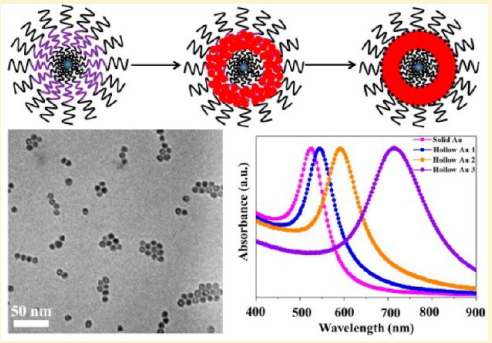

INTRODUCTION

The past several decades have witnessed a rapid revolution in the synthesis of nanocrystals with a diverse spectrum of sizes, shapes, and structures including solid nanoparticles (NPs),[1] nanoprisms,[1,2] nanocube,[3] nanorods,[4,5] nanowires,[6] nanoplates,[7] hollow NPs,[8−10] and so forth. Among them, hollow NPs represent an intriguing class of nanocrystals due to their larger surface area and lower material density as compared to those of solid NPs of similar size. These advantageous attributes not only enable the saving of materials and thus cost reduction but can also impart structural complexity to the system that provides opportunities for the development of materials with new functionalities and/or improved performance for use in water treatment, surface-enhanced Raman scattering (SERS) spectroscopy, optical devices, controlled delivery, and catalysis.[11] For example, in contrast to solid Pd NPs, hollow Pd NPs have been exploited as an efficient and reusable catalyst in Suzuki coupling reactions as a high surface-to-volume ratio of hollow NPs results in more Pd atoms on the surface available for catalysis.[12]

Several impressive approaches have been developed to produce hollow NPs. The most common approach for hollow NPs is based on the use of sacrificial templates by depositing thin metal layers on either preformed hard template (e.g., silica[13] and polymer beads[14]) or soft template (e.g., microemulsions,[15] gas bubbles,[16] and micelles[17]). However, hollow NPs prepared by this approach are usually larger than 50 nm because it is difficult to obtain smaller-sized templates for use. Furthermore, the procedure for selective removal of rigid templates for hollow interiors often introduces uncontrollable compositional and structural complexity, thereby leading to NPs with partial coverage, inhomogeneous shell thickness, poorly defined composition, and so forth.[18,19] In recent years, self-organizations (i.e., template-free) based on nanoscale Kirkendall effect,[20−22] Ostwald ripening,[23] and galvanic replacement[24,25] have emerged as effective routes to hollow NPs. However, the size of NPs resulting from Ostwald ripening

Received: May 3, 2017
Published: August 28, 2017

DOI: 10.1021/jacs.7b04545
J. Am. Chem. Soc. 2017, 139, 12956−12967

Scheme 1. Synthetic Route to Hairy Hollow Plasmonic Nanoparticles (i.e., PS-Capped Hollow Au and Ag Nanoparticles (NPs)) Crafted by Capitalizing on Amphiphilic Star-Like PS-*b*-PAA-*b*-PS Triblock Copolymers as Nanoreactors with Synthesis of (a) Star-Like PS-*b*-P*t*BA-*b*-PS and (b) PS-Capped Hollow Plasmonic NPs

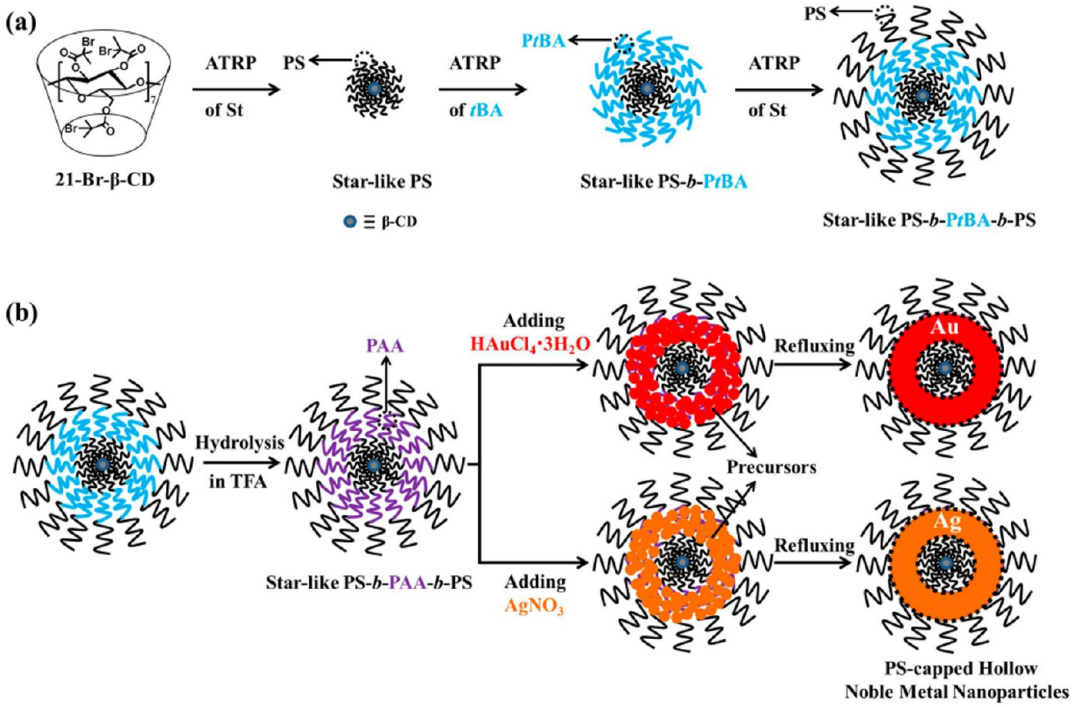

is generally larger than 100 nm.[26] Moreover, it is notable that the template-free approaches noted above are generally material specific. For example, Ostwald ripening and Kirkendall effect often occur in metal-containing compounds (e.g., CoSe[22]), whereas galvanic replacement is applicable primarily to the formation of a limited set of metals and metal alloys.[21−25] In the latter context, although galvanic replacement has been a widely used approach to yield hollow Au and Ag NPs by utilizing a sacrificial metal whose redox potential is more negative than those of the $AuCl_4^-$/Au and Ag^+/Ag pairs, respectively,[18,19,24] the fast interdiffusion between the sacrificial metal and epitaxially deposited metals (i.e., Au and Ag) unavoidably leads to the formation of hollow NPs with the shell composed of metal alloy instead of pure single-component metal.[18] Notably, the sacrificial metal within the formed shell can be selectively and completely removed via the so-called dealloying process. However, it causes a morphological reconstruction, forming nanopores within the shell of the resulting hollow NPs. In addition to the largely limited material choices, all approaches (template and template-free) described above lack precise control over the shell thickness of hollow NPs. It is also noteworthy that as-synthesized hollow NPs are capped with small molecular ligands; agglomeration may thus occur over a long period of time due to the dissociation of the surface ligands upon the change in experimental conditions (e.g., pH, temperature, UV irradiation, etc.).[27] Consequently, limitations such as broader surface plasmon resonance (SPR) peak and premature release when delivering guest compounds may occur. Clearly, the ability to create hollow NPs of a broad variety of materials and precisely controlled dimensions that are intimately and stably capped with ligands is still a challenging issue.

Herein, we develop a general and highly viable strategy for crafting hairy permanently ligated hollow NPs with elaborate control over the hollow interior diameter and shell thickness and thus conveniently tunable optical properties. Central to our strategy is to capitalize on rationally designed amphiphilic star-like triblock copolymers with hydrophilic intermediate block and hydrophobic outer and inner blocks as nanoreactors (i.e., templates) to structure-direct precursors into monodisperse hollow NPs of interest. A series of amphiphilic star-like polystyrene-*block*-poly(acrylic acid)-*block*-polystyrene (denoted PS-*b*-PAA-*b*-PS) triblock copolymers with desired molecular weight (M_n) and low polydispersity index (PDI) are synthesized by sequential atom transfer radical polymerization (ATRP) of styrene (St), *tert*-butyl acrylate (*t*BA), and St monomers, respectively, from the *β*-cyclodextrin-based macroinitiator, followed by hydrolysis of the formed intermediate hydrophobic poly(*tert*-butyl acrylate) (P*t*BA) into hydrophilic poly(acrylic acid) (PAA) blocks. In a mixed solvent containing *N*,*N*-dimethylformamide (DMF) and benzyl alcohol (BA) at a 9:1 volume ratio of DMF/BA, amphiphilic star-like PS-*b*-PAA-*b*-PS triblock copolymers form stable spherical unimolecular micelles comprising the expanded intermediate PAA chains and the collapsed inner and outer PS chains as DMF is a good solvent for both PAA and PS chains whereas BA is a good solvent for PAA and nonsolvent for PS chains. The strong interaction between carboxylic acid groups of PAA blocks and the metal moieties of precursors (i.e., direct coordination with $HAuCl_4$ and electrostatic interaction with $AgNO_3$), together with the unimolecular micellar-like PAA-containing compartment that can accommodate a large volume of precursors due to the expanded chain conformation, leads to the nucleation and growth of PS-capped hollow NPs (i.e., Au and Ag). This strategy contrasts starkly with the approaches described above. Given the living characteristic of ATRP, the molecular weight (i.e., length) of each block (i.e., inner PS, intermediate P*t*BA and hydrolyzed into PAA, and outer PS) with low PDI can be

DOI: 10.1021/jacs.7b04545
J. Am. Chem. Soc. 2017, 139, 12956−12967

readily achieved by controlling their respective ATRP time. This in turn renders convenient control over the diameter of hollow interior and the shell thickness of hollow NPs dictated by the lengths of inner PS and intermediate PAA, respectively, thereby leading to tunable surface plasmon resonance of NPs as corroborated by an integrated experimental and modeling study. It is also worth noting that the outer PS chains that are permanently ligated on the surface of hollow NPs (i.e., hairy hollow NPs) effectively prevent the aggregation of NPs and thus entail their excellent solubility in nonpolar solvents and uniform distribution in polymer matrix. The hollow NPs can be exploited as effective nanocarriers, which combined with their optical properties from visible to near-infrared (near-IR; transparent window for biological systems[28,29]) region and stability, may facilitate potential applications in SERS, catalysis, nanocomposites, biology, and so forth. In addition to Au and Ag hollow NPs demonstrated here, the star-like triblock copolymer nanoreactor strategy can be employed to craft an array of hollow NPs (e.g., semiconducting NPs[30]) of different dimensions, compositions, and functionalities for a wide range of technological applications.

RESULTS AND DISCUSSION

Scheme 1 depicts the synthetic strategy for crafting hairy hollow noble metal NPs (i.e., PS-capped hollow plasmonic NPs) by capitalizing on amphiphilic unimolecular star-like PS-*b*-PAA-*b*-PS triblock copolymers as templates (see Experimental Section). 21-Br-*β*-CD macroinitiator (first panel in Scheme 1a) was first synthesized by esterifying 21 hydroxyl groups of *β*-cyclodextrin (*β*-CD) into bromine groups.[31−35] Emanating from the 21-Br-*β*-CD macroinitiator, unimolecular star-like polystyrene-*block*-poly(*tert*-butyl acrylate)-*block*-polystyrene (PS-*b*-P*t*BA-*b*-PS) triblock copolymers with well-defined molecular weights and low PDI for each block were then prepared by sequential ATRP of styrene (St), *tert*-butyl acrylate (*t*BA), and St monomers (panels 2−4 in Scheme 1a for star-like PS, PS-*b*-P*t*BA, and PS-*b*-P*t*BA-*b*-PS, respectively). The proton NMR (^{1}H NMR) spectra confirm the successful synthesis of star-like PS, PS-*b*-P*t*BA, and PS-*b*-P*t*BA-*b*-PS (Figures S1−S3). Subsequently, the intermediate hydrophobic P*t*BA blocks were hydrolyzed into hydrophilic PAA blocks, thereby yielding amphiphilic star-like PS-*b*-PAA-*b*-PS (second panel in Scheme 1b; Figure S4).

It is worth noting that, in sharp contrast to conventional micelles self-assembled from linear amphiphilic block copolymers due to weak interactions (e.g., van der Waals, hydrogen bonds),[31,33,36] in the present study unimolecular micelles of amphiphilic star-like triblock copolymers are capable of maintaining the compact spherical architecture as three dissimilar blocks strongly and covalently connected to one another (i.e., PS-*b*-PAA-*b*-PS) are tethered to the 21-Br-*β*-CD core (Scheme 1). The resulting amphiphilic star-like PS-*b*-PAA-*b*-PS triblock copolymers were then utilized as nanoreactors for in situ crafting of uniform hollow plasmonic Au and Ag NPs. The reaction was performed in a mixed solvent composed of DMF and BA (9:1 DMF/BA, v/v) (see Experimental Section). Compared with DMF, which is a good solvent for both PAA and PS, BA is a poor solvent for PS yet a good solvent for PAA. As a result, stable unimolecular micelles with well-defined spherical shape consisting of the expanded intermediate PAA chains and the collapsed inner and outer PS chains were formed in 9:1 DMF/BA. The noble metal precursors $HAuCl_4 \cdot 3H_2O$ or $AgNO_3$ were added to the star-like PS-*b*-PAA-*b*-PS DMF/BA solution under stirring. The metal moieties of precursors underwent a strong interaction with carboxyl groups of PAA and thus populated preferentially in the regime comprising the expanded intermediate PAA chains instead of the collapsed inner and outer PS chains (third panels in Scheme 1b). The subsequent addition of respective reducers led to the nucleation and growth of hollow Au or Ag NPs permanently ligated by the collapsed PS chains on their surface (i.e., yielding PS-capped Au and Ag NPs; right panels in Scheme 1b; see Experimental Section). The living characteristic of ATRP imparts the synthesis of polymers with well-defined molecular weight and low PDI.[37] Thus, the length of each block in star-like PS-*b*-PAA-*b*-PS can be readily and precisely tailored by varying the ATRP time, which in turn determines the size of the formed plasmonic NPs and the diameter of hollow interior templated by the intermediate PAA and the inner PS blocks, respectively, although the inner PS chains contract slightly in the 9:1 DMF/BA mixed solvent. The molecular weights of the inner PS, intermediate PAA, and outer PS blocks in star-like PS-*b*-PAA-*b*-PS triblock copolymers and the corresponding dimensions of PS-capped hollow noble metal NPs are summarized in Table S1.

Prior to synthesis of hollow noble metal NPs, amphiphilic star-like PS-*b*-PAA-*b*-PS triblock copolymers were properly stained by uranyl acetate to examine the structure of as-prepared nanoreactors. The dark ringlike nano-objects in Figure 1 corresponding to the intermediate hydrophilic PAA blocks were preferentially stained by uranyl acetate. Compared to the uniform spherical unimolecular micellar-like conformation in solution, star-like PS-*b*-PAA-*b*-PS triblock copolymers have a tendency to lay flat when absorbed on the TEM grid (i.e., solid state), causing the slightly nonuniform morphology.[38−40]

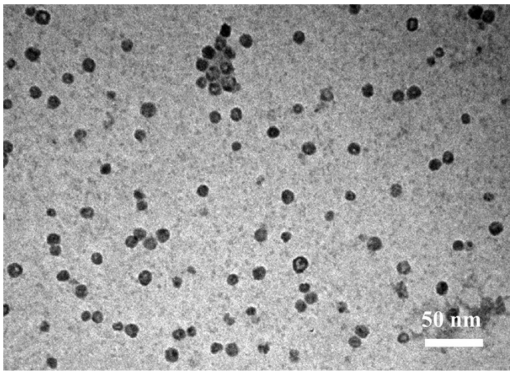

Figure 1. TEM image of amphiphilic star-like PS-*b*-PAA-*b*-PS triblock copolymers (i.e., sample B in Table S1), where PAA blocks are selectively stained by uranyl acetate.

Subsequently, star-like PS-*b*-PAA-*b*-PS triblock copolymers were exploited as nanoreactors for synthesis of uniform PS-capped hollow NPs (i.e., hairy permanently ligated hollow NPs). The carboxylic acid (-COOH) group in the PAA block can associate with $HAuCl_4$ via direct coordination (Figure S5a). This selective interaction has been reported (e.g., carboxylic acid group in either polyacids[41,42] and citric acid[43]). On the other hand, the anionic side groups ($-COO^-$) in PAA block from deprotonation of -COOH groups and the cations of precursor (Ag^+) can form ion pair through electrostatic interactions (Figure S5b). Similarly, poly-4-vinylpyridine (P4VP) was also used to interact with the cations of precursor

DOI: 10.1021/jacs.7b04545
J. Am. Chem. Soc. 2017, 139, 12956−12967

(e.g., Ag^+) via direct coordination or the anions of precursor (e.g., $AuCl_4^-$) through protonation (i.e., electrostatic interaction).[44,45] To better understand the interactions noted above, we performed TEM measurements on star-like PS-*b*-PAA-*b*-PS copolymers (i.e., sample B in Table S1) after associating with $HAuCl_4$ and $AgNO_3$. Ten-times of precursors over AA units was employed to ensure the maximum incorporation of precursors into the PAA compartment, as an insufficient amount of precursors in the PAA compartment resulted in irregular nanostructures or nanoclusters instead of spherical NPs as discussed in our previous work[46] and elsewhere.[47,48] Notably, even without staining, the PAA compartment impregnated with $HAuCl_4$ and $AgNO_3$ were clearly evident in Figure S6a and b, respectively, due to high electron density of the metal moieties. In addition, compared with pure star-like copolymer (Figure 1), the PAA/$HAuCl_4$ and PAA/$AgNO_3$ complexes possessed spherical shape with uniform size[40] (Figure S6). During the reaction, the excess precursors formed big bulk inorganic materials outside nanoreactors as there were no free ligands in solution and tended to precipitate on the bottom, which can be removed by ultracentrifugation after reaction (Experimental Section).

Figure 2 shows the TEM images of PS-capped hollow Au and Ag NPs. By utilizing two star-like PS-*b*-PAA-*b*-PS triblock copolymers with rationally designed molecular weights of each block (samples A and B in Table S1), monodisperse hollow Au NPs with an external diameter of 12 ± 0.4 nm and shell thickness of 4.7 ± 0.3 nm (denoted hollow Au 1) and an external diameter of 12 ± 0.5 nm and shell thickness of 2.7 ± 0.2 nm (denoted hollow Au 2), respectively, were yielded (Figure 2a–d).

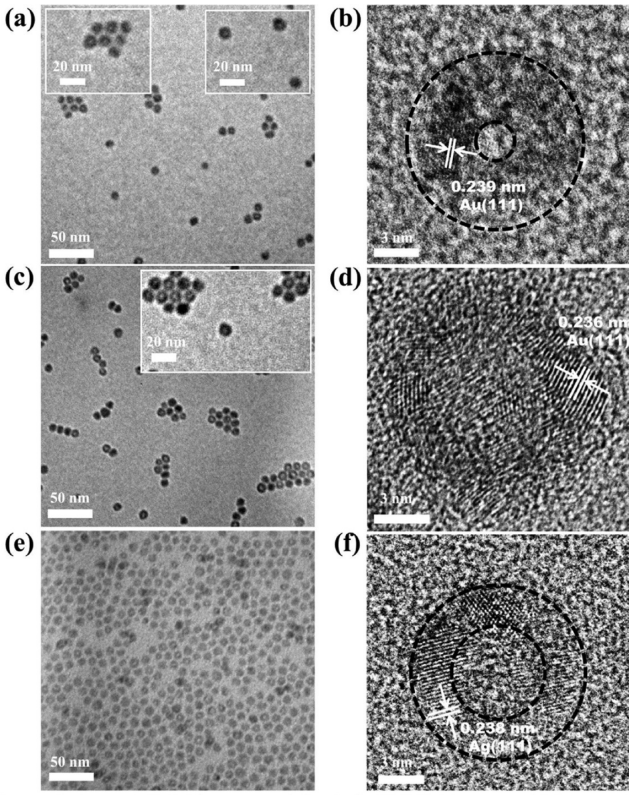

Figure 2. (a, c, e) TEM and (b, d, f) HRTEM images of PS-capped hollow noble metal NPs crafted by employing amphiphilic star-like PS-*b*-PAA-*b*-PS triblock copolymers as nanoreactors. (a–d) PS-capped hollow Au NPs with (a, b) an external diameter of 12 ± 0.4 nm and shell thickness of 4.7 ± 0.3 nm (i.e., hollow Au 1) and (c, d) an external diameter of 12 ± 0.5 nm and shell thickness of 2.7 ± 0.2 nm (i.e., hollow Au 2). (e, f) PS-capped hollow Ag NPs with an external diameter of 11.6 ± 0.4 nm and shell thickness of 2.7 ± 0.3 nm (i.e., hollow Ag). Scale bars in (b, d, f) are 3 nm.

In comparison to hollow Au NPs, research on hollow Ag NPs is rather limited in the literature.[49,50] Ag NPs carry several advantages over Au NPs. First, Ag precursors (e.g., $AgNO_3$) are much less expensive than Au precursors (e.g., $HAuCl_4{\cdot}3H_2O$) thus reducing the cost of Ag NPs for applications compared to Au NPs of similar performance. Second, Ag NPs possess more effective antibacterial[51] and photothermal[52] properties than Au NPs. In this context, hollow Ag NPs with an external diameter of 11.6 ± 0.4 nm and shell thickness of 2.7 ± 0.3 nm (denoted Hollow Ag) was also crafted using the same nanoreactor (i.e., sample B in Table S1) as shown in Figure 2e and f. The center of these NPs appeared relatively bright, indicating they are hollow (Figure 2a, c, and e), which were further substantiated by high-resolution TEM imaging (Figure 2b, d, and f). The hollow Au and Ag NPs showed the lattice-fringe distances of 2.4 Å, which match well with the (111) plane of the face-centered cubic (fcc) Au and Ag crystals. As hollow NPs differed from nanorings, lattice fringes may also be observed in the center (i.e., hollow interior) of NPs under TEM, which can be attributed to the crystalline shell right above the center hollow interior.[22,53] Clearly, the Au and Ag shells are polycrystalline, which may be rationalized as follows. As described above, Au and Ag NPs were formed and encapsulated within the compartment occupied by PAA blocks due to the strong interaction between noble metal moieties of $HAuCl_4{\cdot}3H_2O$ or $AgNO_3$ precursors and carboxylic acid groups of PAA blocks together with the unimolecular micellar-like PAA-containing compartment that can accommodate a large volume of precursors due to the expanded chain conformation of PAA blocks. We note that the PAA chain segments may still reside during crystallization. The nanocrystals on the adjacent PAA segments arrange at a planar interface and share a crystallographic alignment via an oriented attachment mechanism.[54] For the overall energy to be minimzed, a polycrystalline shell with incompletely coordinated surface atoms was formed accompanied by the reduced energy penalty.[54] The dimension distribution histograms of PS-capped hollow Au and Ag NPs obtained by analyzing large-area TEM images (Figure 4) are shown in Figure 3, suggesting that monodisperse NPs were achieved. The internal and external diameters of the resulting hollow NPs are slightly smaller than the hydrodynamic diameters of the corresponding star-like PS and PS-*b*-PAA measured in DMF (Table S2), respectively, likely due to the use of 9:1 DMF/BA as a mixed solvent in the reaction as well as the slight volume contraction of the compartment comprising PAA chains during the crystallization of NPs. The interparticle distance of hollow Au NPs was smaller than that of hollow Ag NPs (Figures 2 and 4). This is because the Au surface is hydrophobic whereas the Ag surface is hydrophilic due to the formation of an ultrathin silver oxide layer on the surface,[55] leading to different conformations of the outer PS chains in these two cases. On the other hand, atomic force microscopy (AFM) measurements were performed to study the conformation change of the outer PS chains on the surface of Au and Ag hollow NPs (Figure S7). We note that the lateral diameter of an individual NP measured by AFM was much larger than the size obtained by TEM. This can be ascribed to

DOI: 10.1021/jacs.7b04545
J. Am. Chem. Soc. 2017, 139, 12956–12967

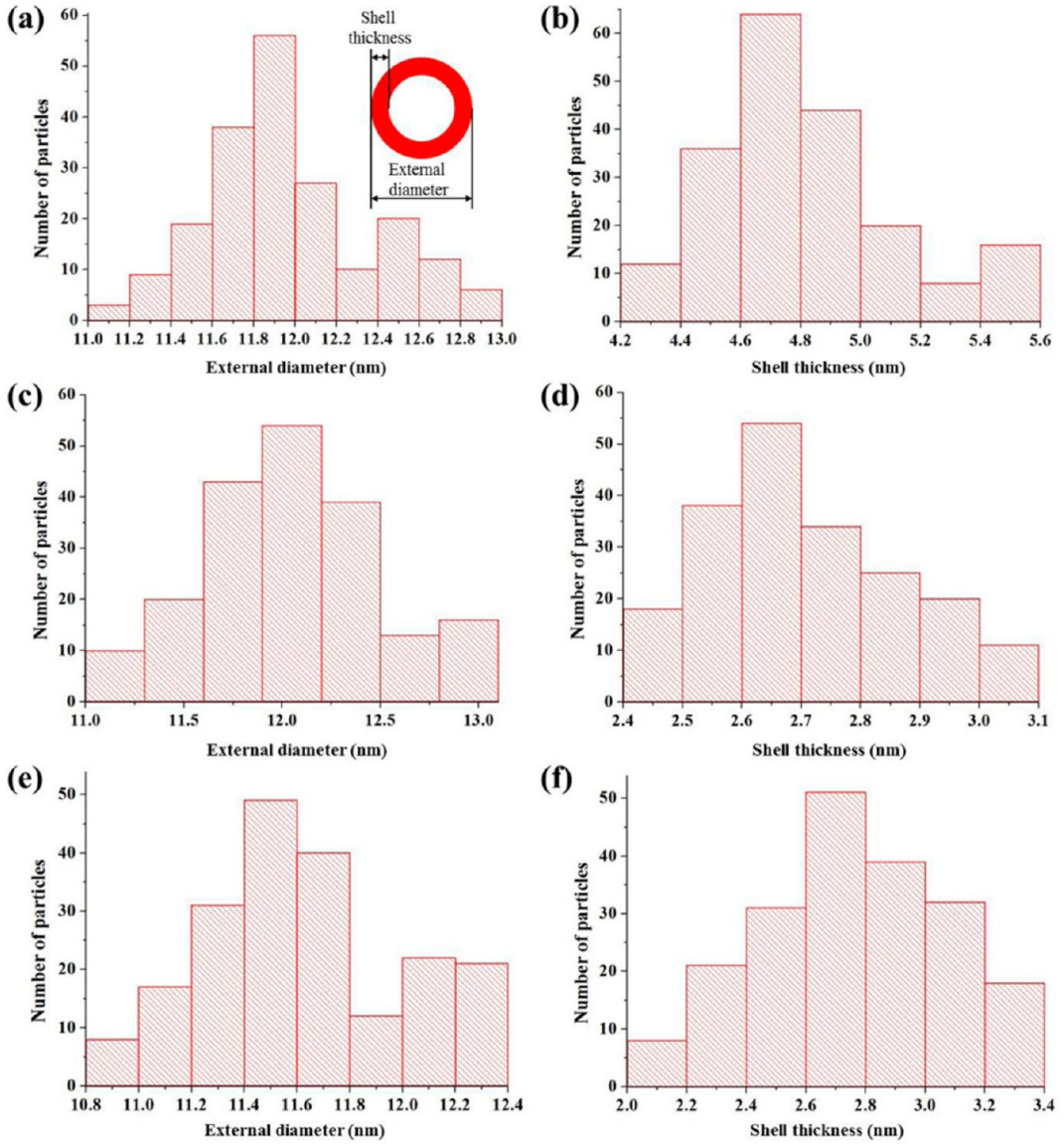

Figure 3. Histograms of the dimension distributions of 200 randomly selected NPs from TEM images in Figure 4. PS-capped hollow Au NPs with (a) an external diameter of 12 ± 0.4 nm and (b) shell thickness of 4.7 ± 0.3 nm (i.e., hollow Au 1), (c) an external diameter of 12 ± 0.5 nm and (d) shell thickness of 2.7 ± 0.2 nm (i.e., hollow Au 2), and PS-capped hollow Ag NPs with (e) an external diameter of 11.6 ± 0.4 nm and (f) shell thickness of 2.7 ± 0.3 nm (i.e., hollow Ag).

the AFM tip convolution as the radius of curvature of the AFM tip used is 20 nm.[36] The height in the case of hollow Au NPs was approximately 12.6 nm (Figure S7a and c), whereas it was roughly 14.5 nm for hollow Ag NPs (Figure S7b and d). The external diameters were 12 nm for hollow Au NPs and 11.6 nm for Ag NPs; thus, the PS chains situated on their surfaces were 0.6 and 2.9 nm, respectively, due to the dissimilar conformation of PS chains even with the same molecular weight of PS, as noted above. This is in good agreement with the TEM measurements.

It is notable that micelles formed by self-assembly of amphiphilic linear block copolymers in selective solvents have been used as nanoreactors for in situ growth of hollow NPs.[40,50] However, as noted above, these linear block copolymer micelles depend sensitively on the experimental conditions (e.g., pH, temperature, solvent, etc.). A change in these parameters may likely induce a variation in size, shape, and stability of linear block copolymer micelles,[56] leading to the formation of irregular hollow NPs or aggregates. This may, for instance, result in a broader SPR peak and trigger uncontrolled release during the delivery of guest compounds. In sharp contrast, the implementation of star-like triblock copolymer nanoreactors rendered the production of hairy uniform permanently ligated hollow nanoparticles with precisely controlled dimensions (Figures 2 and 4).

For a better comparison, PS-capped solid Au and Ag NPs of similar diameters to the external diameters of hollow NPs were also synthesized.[33] The monodisperse PS-capped solid Au and Ag NPs with average diameters of 12.2 ± 0.5 nm and 11.9 ± 0.3 nm, respectively, are clearly evident (Figure 5). No hollow structures were observed from the zoom-in images. On the basis of the nitrogen adsorption−desorption (Figure S8), the surface area of hollow Au NPs was 86.2 m^2 g^{-1} compared to that of 39.1 m^2 g^{-1} in the corresponding solid Au NPs with the same external diameter. This result substantiated that the shell of as-prepared hollow NPs was not completely sealed and PS

DOI: 10.1021/jacs.7b04545
J. Am. Chem. Soc. 2017, 139, 12956−12967

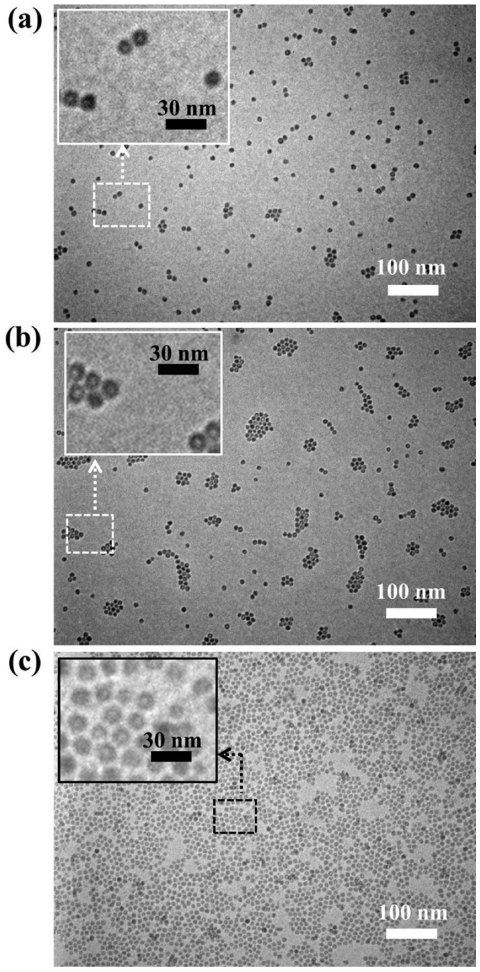

Figure 4. TEM images of PS-capped hollow Au NPs over a large area with (a) an external diameter of 12 ± 0.4 nm and shell thickness of 4.7 ± 0.3 nm (i.e., hollow Au 1), (b) an external diameter of 12 ± 0.5 nm and shell thickness of 2.7 ± 0.2 nm (i.e., hollow Au 2), and PS-capped hollow Ag NPs with (c) an external diameter of 11.6 ± 0.4 nm and shell thickness of 2.7 ± 0.3 nm (i.e., hollow Ag). Insets are zoom-in images.

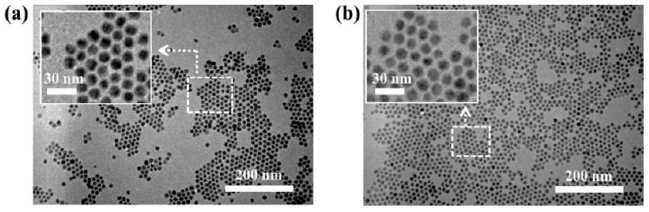

Figure 5. TEM images of PS-capped (a) solid Au NPs with an average diameter of 12.2 ± 0.5 nm (i.e., solid Au) and (b) PS-capped solid Ag NPs with an average diameter of 11.9 ± 0.3 nm (i.e., solid Ag). Insets are zoom-in images.

chains inside the hollow interior may shrink at dry state, leading to a higher accessible surface area than that of solid NPs. This renders hollow NPs for promising applications in catalysis, guest molecule delivery, and so forth.

Figure 6 compares the XRD patterns of PS-capped hollow and solid plasmonic NPs. The peaks from PS-capped hollow Au NPs at the 2θ scattering angles of 37.74°, 44.01°, 64.42°, 77.27°, and 81.31° correlate to the diffractions from the (111), (200), (220), (311), and (222) planes of fcc Au crystals, respectively (Figure 6a). Compared with solid Au NPs of similar size (i.e., solid Au), the slightly broadened peaks of hollow Au NPs (i.e., hollow Au 1 and hollow Au 2) can be attributed to the structural difference (i.e., hollow vs solid).[53] On the other hand, the peaks became broader as the shell thickness decreased, signifying the smaller grain size of Au within the thinner shell (hollow Au 2). This is in good agreement with the HRTEM images in Figure 2. A similar observation was found on the XRD pattern of PS-capped hollow Ag NPs (Figure 6b). Clearly, the XRD measurements confirmed that the formed hollow Au and Ag NPs are crystalline.

The SPR properties of PS-capped hollow Au and Ag NPs in toluene were scrutinized by UV−vis measurements. The plasmonic properties of solid noble metal NPs as a function of NP diameter has been systematically studied, where the variation in plasmonic absorption maximum was found to be rather limited.[33] In addition to the size effect,[33] the NP structure (i.e., hollow vs solid) also exerts a significant influence on the SPR property. To explore the effect of shell thickness of hollow noble metal NPs on the SPR property, we kept the external diameter of as-prepared hollow NPs constant while varying the shell thickness. For comparison, the absorption spectra of PS-capped solid Au and Ag NPs with nearly the same diameter (i.e., ∼12 nm) are shown in Figure 7. The 12 nm PS-capped solid Au and Ag NPs exhibited strong characteristic SPR peaks at approximately 525 and 420 nm, respectively, which are in a good agreement with the previous work.[57] Notably, when a small hollow interior is present in solid Au NPs (i.e., hollow Au 1 with a shell thickness of 4.7 nm in Figure 7a), the SPR peak shifted from 525 to 545 nm, which is typically the peak position for solid Au NPs with a diameter larger than 50 nm.[57] Clearly, as the external diameter of hollow Au 1 is nearly identical to the diameter of solid Au, a 20 nm red-shift in SPR peak results from the structural difference between solid and hollow Au NPs. Interestingly, the SPR peak was further red-shifted to 592 nm when the shell thickness progressively decreased to 2.7 nm (i.e., hollow Au 2 in Figure 7a). In stark contrast to the SPR spectra of hollow Au NPs synthesized from the replacement reaction,[18,19,24,25] the SPR peaks in the present study are much narrower, suggesting the high uniformity of hollow NPs, which is consistent with the TEM results in Figure 2. Moreover, in the case of hollow NPs dynamically capped with small molecular ligands, ligands may dissociate from the shell surface after a long period of time or under varied experimental conditions (e.g., temperature higher than 60 °C can break the Au−S bonds).[27] To this end, hollow NPs yielded by a nanoreactor strategy showed premium stability for a long time and under high temperature (Figure S9) as the outer PS chains are permanently ligated on the surface. A similar case was also observed in hollow Ag NPs (Figure 7b). The hollow Ag NPs with a shell thickness of 2.7 nm displayed a distinct SPR peak at approximately 462 nm (i.e., hollow Ag in Figure 7b), which differed greatly from solid Ag NPs with the similar diameter located at 420 nm. The SPR band can be attributed to the oscillations of free electrons upon light irradiation.[57] In the case of hollow noble metal NPs, the electromagnetic field of incident light induces surface charges at both the inner and outer surfaces of the shell, which lead to the nanocavity plasmons and nanosphere surface plasmons, respectively,[13] as depicted in Figure 8. The finite shell thickness facilitates the interaction between nanocavity and nanosphere plasmons, thereby resulting in two new hybridized resonances,

DOI: 10.1021/jacs.7b04545
J. Am. Chem. Soc. 2017, 139, 12956−12967

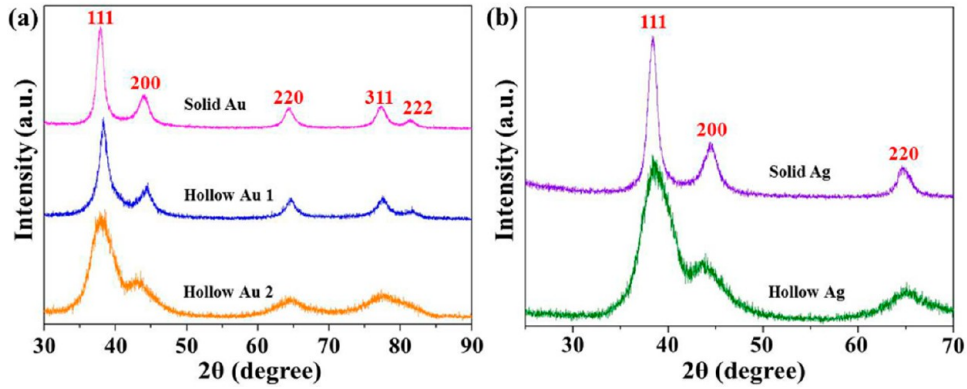

Figure 6. XRD patterns of (a) PS-capped solid Au NPs (i.e., solid Au) and PS-capped hollow Au NPs (i.e., hollow Au 1 and hollow Au 2) and (b) PS-capped solid Ag NPs (i.e., solid Ag) and PS-capped hollow Ag NPs (i.e., hollow Ag).

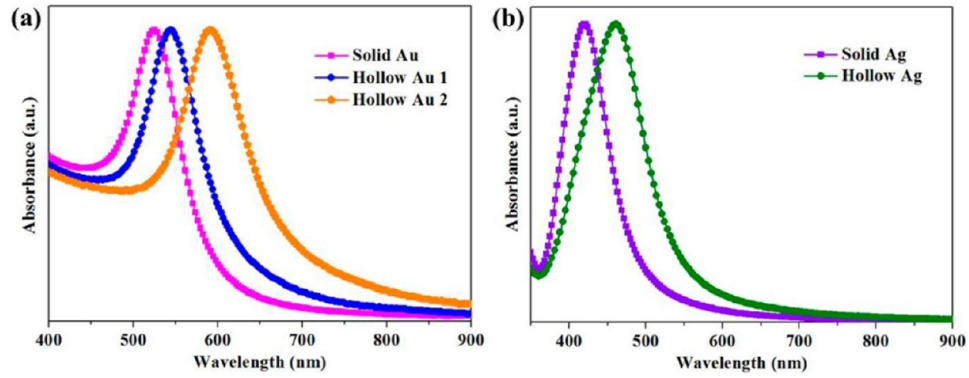

Figure 7. UV−vis spectra of (a) PS-capped solid Au NPs with a diameter of 12.2 ± 0.5 nm (i.e., solid Au) and PS-capped hollow Au NPs (i.e., hollow Au 1 with an external diameter of 12 ± 0.4 nm and shell thickness of 4.7 ± 0.3 nm and hollow Au 2 with an external diameter of 12 ± 0.5 nm and shell thickness of 2.7 ± 0.2 nm) and (b) PS-capped solid Ag NPs with a diameter of 11.9 ± 0.3 nm (i.e., solid Ag) and PS-capped hollow Ag NPs with an external diameter of 11.6 ± 0.4 nm and shell thickness of 2.7 ± 0.3 nm (i.e., hollow Ag).

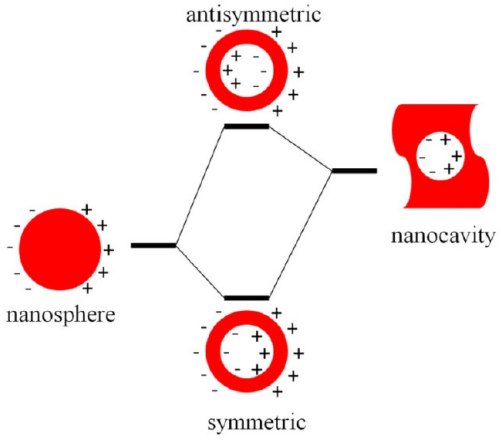

Figure 8. Schematic illustration of the energy level of plasmon hybridization[13] in hollow NPs. The interaction between the nanosphere and nanocavity plasmons results in two new hybridized resonances, that is, a higher energy antisymmetric plasmon and a lower energy symmetric plasmon.

that is, a higher energy plasmon from the antisymmetric combination or a lower energy plasmon from the symmetric combination.[58] The lower energy plasmon interacts strongly with the incident light whereas the higher energy one interacts weakly,[59] causing the red-shift of SPR peak positions. On the other hand, the shell thickness (e.g., 4.7 nm Au shell and 2.7 nm Ag shell), which is much smaller than the mean free path (~50 nm) of electrons in the bulk Au and Ag, dictates the strength of the interaction between nanocavity and nanosphere plasmons.[13] For hollow NPs with thinner shells (i.e., 2.7 nm Au shell), a stronger interaction between nanocavity and nanosphere plasmons gives rise to a much more significant charge separation and a greater red-shift,[13] as evidenced in Figure 7.

To better understand the influence of the shell thickness of hollow NPs on their SPR properties, we performed the simulation of absorption cross sections of hollow Au and Ag NPs. On the basis of the TEM studies of as-prepared hollow NPs, the geometric model in a typical simulation was constructed as a spherical shape in the two-dimensional axisymmetric coordinate (Figure S10a). The external diameters for Au and Ag NPs were set at 12 and 11.6 nm, respectively, with varied shell thicknesses. The medium surrounding hollow NPs was assumed to be toluene with an infinite thickness, and the hollow interior of NPs was assumed to be filled with PS chains. A representative example of the surface mesh discretization and the optical field distribution of hollow noble metal NPs is shown in Figure S10b. There are large field enhancements both outside and inside hollow NPs. For the outside optical field, the points of the largest enhancement occur along the polarization direction, whereas inside the cavity they are perpendicular to that direction. This can be attributed to the structural effect (i.e., hollow structure) of NPs in response to the incident light.[60]

DOI: 10.1021/jacs.7b04545
J. Am. Chem. Soc. 2017, 139, 12956−12967

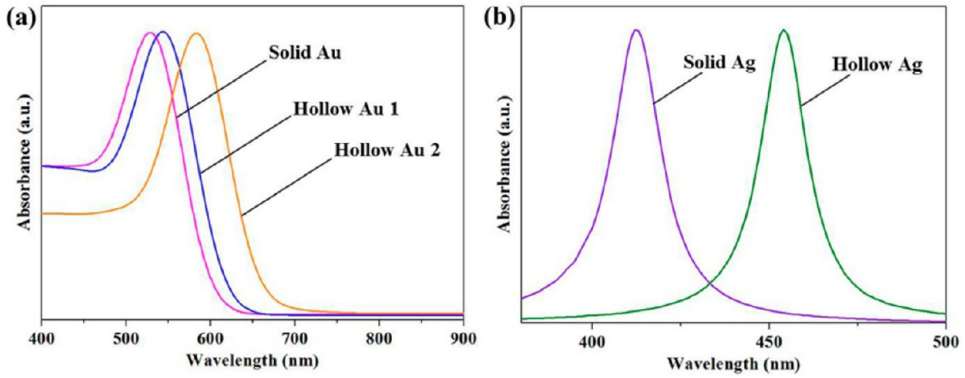

Figure 9. SPR simulations of (a) PS-capped solid Au NPs with a diameter of 12.2 ± 0.5 nm (i.e., solid Au) and PS-capped hollow Au NPs (i.e., hollow Au 1 with an external diameter of 12 ± 0.4 nm and shell thickness of 4.7 ± 0.3 nm and hollow Au 2 with an external diameter of 12 ± 0.5 nm and shell thickness of 2.7 ± 0.2 nm) and (b) PS-capped solid Ag NPs with a diameter of 11.9 ± 0.3 nm (i.e., solid Ag) and PS-capped hollow Ag NPs with an external diameter of 11.6 ± 0.4 nm and shell thickness of 2.7 ± 0.3 nm (i.e., hollow Ag).

We note that either discrete dipole approximation (DDA)[19] or the finite element method (FEM)[42] have been reported to quantify the optical properties of NPs with complex structures (e.g., hollow). In comparison to DDA, FEM chosen in the present work enables an easy calculation of NPs with a complex structure and arbitrary heterogeneity.[42] Figure 9 compares the simulated absorption spectra of hollow Au and Ag NPs as well as the corresponding solid NPs. For Au NPs, the calculated SPR peak shifts from 528 nm for solid NPs to 543 nm for hollow NPs at a shell thickness of 4.7 nm (hollow Au 1 in Figure 9a). As the shell thickness was further decreased to 2.7 nm (i.e., hollow Au 2), a larger red-shift to 583 nm was obtained. These calculated results correlated well with the experimental observations in Figure 7a. To provide more useful insight into the relationship between the plasmon properties and the shell thickness of noble metal NPs, we also conducted calculations with varied shell thicknesses, which are summarized in Table S3. By fixing the external diameter (i.e., 12 nm), the SPR peak positions of hollow Au NPs red-shift as the shell thickness decreases (Figure S11). When the shell thickness is close to the external radius (i.e., small hollow interior), there are only small shifts in the SPR peak position. For instance, the SPR peak marginally varies from 542 to 543 nm when the shell thickness decreases from 4.9 to 4.7 nm. However, the same decrease for the thinner shell thickness (i.e., large hollow interior) from 2.9 to 2.7 nm leads to a significant red-shift from 572 to 583 nm (Table S3). This is not surprising as a minor variation in the thickness for thinner shells will trigger the stronger interaction between nanocavity and nanosphere plasmons,[13] resulting in a larger red-shift of SPR peak position as discussed above. As the geometric model for a typical simulation in the present work was a spherical shape with sealed surface, the simulated SPR peaks of hollow NPs were slightly blue-shifted compared to those of experimental SPR peaks as expected. The simulation on hollow Ag NPs (Figure 9b) also agreed well with the experimental observations in Figure 7b, where the same trend of the shell thickness effect was also seen in hollow Ag NPs (Table S4 and Figure S12). For example, a change from 2.8 to 2.6 nm in the shell thickness of hollow Ag NPs induces a 9 nm increase in SPR peak position whereas the same amount of decrease from 2.5 to 2.3 nm causes a larger, up to 11 nm, red-shift. Taken together, the integrated experimental and modeling study clearly demonstrated that it is viable to precisely tailor the SPR properties by systematically tuning the shell thickness of hollow plasmonic NPs enabled by the star-like block copolymer nanoreactor strategy.

In addition to the effect of shell thickness, we also investigated the influence of external diameter of hollow NPs on optical properties. Hollow Au NPs with an external diameter of 25.1 ± 1.8 nm and shell thickness of 3.1 ± 0.4 nm (i.e., hollow Au 3; Figure S13a) were synthesized by exploiting a larger-sized star-like copolymer nanoreactor (sample C in Table S1). Compared with hollow Au 2, hollow Au 3 NPs possessed a similar shell thickness but a larger external diameter, causing a further red-shift of the SPR peak from 592 nm (for hollow Au 2) to 711 nm (for hollow Au 3) (Figure S13b), which agreed well with the simulated value (702 nm). It is interesting to note that blood and soft tissues are highly transparent in the near-IR region (700−1000 nm) due to the greatly reduced attenuation of light through these biological systems.[28,29] This makes hollow Au NPs attractive in bioimaging as well as biomedical diagnosis and therapy.

NPs with hollow interior and unsealed shell can be exploited as effective nanocarriers to deliver and release numerous guest molecules. To this end, Rhodamine B (RhB, a fluorescent dye) and as-prepared hollow Au 2 were chosen as a model guest compound and nanocarrier, respectively, to prove the capability of molecule release. The dyes and hollow Au 2 NPs were dispersed in $CHCl_3$ under stirring to load RhB. As $CHCl_3$ is a good solvent for PS, the outer PS chains extended and RhB molecules diffused through the unsealed shell into the hollow interior (first panel in Figure 10a). After RhB molecules were loaded within hollow Au NPs, the poor solvent (i.e., methanol) of PS was added to the system. As a result, RhB molecules were trapped within hollow Au NPs by the collapsed outer PS chains on the unsealed NP surface (second panel in Figure 10a). After collection and washing by centrifugation, hollow Au NPs loaded with RhB molecules were redispersed in $CHCl_3$. As $CHCl_3$ renders PS chains to recover to their extended conformation, RhB molecules can diffuse into the surrounding solvent (third panel in Figure 10a). At different desired times, methanol was added to the solution, and hollow NPs were centrifuged to obtain the supernatant. The release behavior of RhB molecules can be readily tracked by recording the UV−vis spectra of the supernatants at different times because RhB has a characteristic absorption peak at approximately 550 nm. The absorption peak intensity progressively increased when nano-

DOI: 10.1021/jacs.7b04545
J. Am. Chem. Soc. 2017, 139, 12956−12967

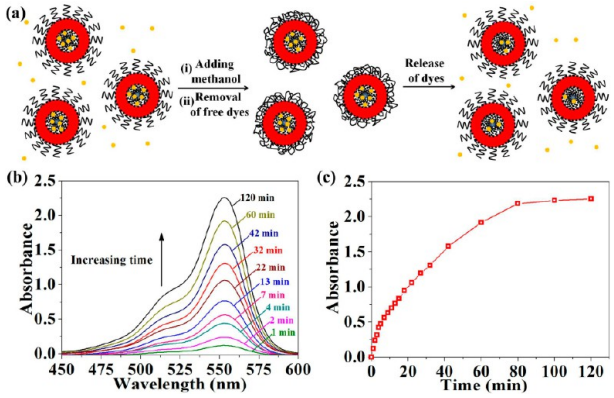

Figure 10. (a) Stepwise representation of encapsulation and release of dyes (RhB) using PS-capped hollow NPs. (b) UV−vis spectra of RhB molecules released from PS-capped hollow NPs at various times. (c) Release kinetics of RhB molecules determined from the absorbance at 550 nm of surpernatant as a function of time.

carriers were redispersed in $CHCl_3$ due to continuous release (Figure 10b). The release kinetics are shown in Figure 10c. The initial high release rate resulted from a huge concentration gradient of RhB molecules between the hollow interior and surrounding solvent. The release rate decreased with time as the concentration gradient gradually became smaller. The release rate was similar to that using a metal−organic framework (MOF) as carrier.[61] Thus, as-prepared hollow NPs were capable of encapsulating and releasing guest compounds. By extension, the outer PS chains can be easily replaced with other functional polymers, for instance, temperature-sensitive polymers triggered by heat or laser. Together with tunable optical properties ranging from visible to near-IR region and premium stability, the nanocarriers may find applications in catalysis and biology. This will be the focus of a future study.

CONCLUSIONS

In summary, we developed a facile star-like triblock copolymer nanoreactor strategy for in situ crafting of hairy uniform hollow plasmonic NPs with precise dimensions, compositions, and tunable optical properties. Specifically, the diameter of hollow interior and shell thickness of NPs can be effectively tailored by tuning the molecular weights of the inner PS and intermediate P*t*BA blocks, respectively, during ATRP for synthesis of star-like PS-*b*-P*t*BA-*b*-PS triblock copolymers. It is important to note that both experiments and simulations on plasmonic properties of hollow NPs correlated well with one another and clearly revealed that the characteristic SPR properties of hollow NPs can be readily adjusted by altering either shell thickness or external diameter. In contrast to solid plasmonic NPs of the same size, the SPR peaks of hollow NPs red-shift, and the magnitude of shift increases with a decreased shell thickness. Quite intriguingly, a subtle variation in shell thickness for the thinner shell invokes a marked red-shift compared to a small red-shift for hollow NPs with the thicker shell. Such easily implemented and tunable SPR properties may greatly expand the applications of hollow plasmonic NPs in catalysis, SERS, imaging, sensors, optics, electronics, and optoelectronics. As these hairy NPs are intimately and permanently ligated by polymer chains on the surface, they possess good solubility of hollow NPs in nonpolar solvents with long-term stability and may enable a homogeneous dispersion in a polymer matrix for use in functional nanocomposites. These hairy permanently ligated hollow NPs may stand out as an efficient class of nanocarriers. Although hollow noble metal NPs are exemplified in this study to show the capability of star-like block copolymer nanoreactor strategy for uniform hairy NPs, virtually a wide range of hollow NPs with precise yet tunable dimensions and versatile functionalities can be created for fundamental understanding of shell thickness and external diameter on physical properties of hollow NPs as well as for targeted applications.

EXPERIMENTAL SECTION

Materials. 2,2′-Bipyridyl (bpy, >99%), *N*,*N*,*N*′,*N*″,*N*″-pentamethyldiethylene triamine (PMDETA, 99%), anhydrous 1-methyl-2-pyrrolidinone (NMP, 99.5%), 2-bromoisobutyryl bromide (98%), trifluoroacetic acid (TFA, 99.9%), gold(III) chloride trihydrate ($HAuCl_4{\cdot}3H_2O$, ≥99.9%), silver nitrate ($AgNO_3$, ≥99.0%), and Rhodamine B (RhB, 95%) were purchased from Sigma-Aldrich and used without further purification. *β*-Cyclodextrin (*β*-CD, Sigma-Aldrich) was dried in a vacuum oven at 80 °C overnight prior to use. CuBr (98%, Sigma-Aldrich) was stirred in acetic acid for 24 h, washed with ethanol and diethyl ether, and dried in a vacuum oven at room temperature. Styrene (St, Sigma-Aldrich, ≥99%) was washed with 10% NaOH aqueous solution and water sequentially, dried over anhydrous $MgSO_4$ and CaH_2 successively, and distilled under reduced pressure. Anisole (TCI America, 99.0%), methyl ethyl ketone (MEK, Fisher Scientific, 99.9%), *tert*-butyl acrylate (*t*BA, Sigma-Aldrich, 98%), and *N*,*N*-dimethylformamide (DMF, Fisher Scientific, 99.9%) were distilled over CaH_2 under reduced pressure prior to use. All other reagents were purified by common purification procedures.

Synthesis of Multiarm, Star-Like Polystyrene (Star-Like PS) Homopolymer via the First ATRP. Heptakis[2,3,6-tri-*O*-(2-bromo-2-methylpropionyl)]-*β*-cyclodextrin (i.e., 21Br-*β*-CD) was first synthesized according to previous reports.[31,33] Star-like PS was then synthesized by atom transfer radical polymerization (ATRP) of St monomers (i.e., the first ATRP) using 21Br-*β*-CD as macroinitiator. Typically, CuBr (70.7 mg), bpy (153.9 mg), 21Br-*β*-CD (100 mg), and St (21 mL) were placed in an ampule purged with argon. The ampule was sealed after being degassed by three freeze−pump−thaw cycles in liquid N_2 and dipped in an oil bath at 90 °C to start the reaction. The reaction was quenched by immersing the ampule in liquid N_2 at different time intervals. The reaction solution was then diluted by THF, passed through a neutral alumina column to remove the catalyst, and purified by fractional precipitation with THF as solvent and methanol/water (1:1, v/v) as precipitator. The product was collected and dried in a vacuum oven at 40 °C for 48 h.

Synthesis of Multiarm, Star-Like Polystyrene-*block*-poly(*tert*-butyl acrylate) (PS-*b*-P*t*BA) (Star-Like PS-*b*-P*t*BA) Diblock Copolymer via the Second ATRP. Star-like PS-*b*-P*t*BA was synthesized via ATRP of *t*BA monomers (i.e., the second ATRP) in MEK using star-like PS as macroinitiator. Briefly, the reaction mixture at *t*BA/star-like PS (i.e., Br group in the macroinitiator)/copper bromide/PMDETA = 800:1:1:2 (molar ratio) in MEK (1 g of *t*BA in 1 mL of solvent) was placed in an ampule purged with argon and degassed by three freeze−pump−thaw cycles in liquid N_2. The ampule was then sealed and dipped in an oil bath at 60 °C to start the reaction. After a desired polymerization time, the reaction was quenched by immersing the ampule in liquid N_2. The raw solution was then diluted by THF and passed through a column of neutral alumina to remove the catalyst and subsequently purified by fractional precipitation with THF as solvent and methanol/water (1:1, v/v) as precipitator. The collected product was dried in a vacuum oven at 40 °C for 48 h.

Synthesis of Multiarm, Star-Like Polystyrene-*block*-poly(*tert*-butyl acrylate)-*block*-polystyrene (PS-*b*-P*t*BA-*b*-PS) (Star-Like PS-*b*-P*t*BA-*b*-PS) Triblock Copolymer via the Third ATRP. Star-like PS-*b*-P*t*BA-*b*-PS was prepared by ATRP of St monomers (i.e., the third ATRP) in anisole using the synthesized star-like PS-*b*-P*t*BA as macroinitiator. Briefly, the reaction mixture with molar ratio of St/star-like PS-*b*-P*t*BA (i.e., Br group in the macroinitiator)/copper

DOI: 10.1021/jacs.7b04545
J. Am. Chem. Soc. 2017, 139, 12956−12967

bromide/PMDETA = 800:1:1:2 in anisole (1 g of St in 1 mL of solvent) was placed in an ampule purged with argon and degassed by three freeze−pump−thaw cycles in liquid N_2. The ampule was then sealed and dipped in an oil bath at 90 °C to start the reaction. After a certain desired time, the reaction was quenched by immersing the ampule in liquid N_2. The crude product was then diluted by THF and passed through a column of neutral alumina to remove the catalyst and subsequently purified by fractional precipitation with THF as solvent and methanol/water (1:1, v/v) as precipitator. The yielded product was collected and dried in a vacuum oven at 40 °C for 48 h.

Synthesis of Amphiphilic Multiarm, Star-Like Polystyrene-*block*-poly(acrylic acid)-*block*-polystyrene (Star-Like PS-*b*-PAA-*b*-PS) Triblock Copolymer by Hydrolysis. A typical hydrolysis process was performed as follows. Star-like PS-*b*-P*t*BA-*b*-PS (500 mg) was thoroughly dissolved in $CHCl_3$ (50 mL) followed by the addition of trifluoroacetic acid (TFA, 5 mL) to start the hydrolysis. After stirred at room temperature for 24 h, the resulting amphiphilic star-like PS-*b*-PAA-*b*-PS triblock copolymer was gradually precipitated in $CHCl_3$. The final product was collected, washed with $CHCl_3$, and thoroughly dried under a vacuum at 40 °C.

Synthesis of PS-Capped Hollow Au Nanoparticles. By exploiting star-like PS-*b*-PAA-*b*-PS triblock copolymers as nanoreactors, PS-capped hollow Au nanoparticles (NPs) were crafted. All the reactions were performed in the 9:1 *N*,*N*-dimethylformamide/benzyl alcohol (DMF/BA) mixed solvent. As DMF is a good solvent for both PAA and PS, whereas BA is a good solvent only for PAA, star-like PS-*b*-PAA-*b*-PS copolymers form stable spherical unimolecular micelles with the expanded intermediate PAA chains and the collapsed inner and outer PS chains. The strong coordination interaction between the metal moieties of Au precursors ($HAuCl_4{\cdot}3H_2O$) and the carboxyl groups of PAA as well as the well-defined micellar structure lead to the selective concentration of Au precursors in the space occupied by the intermediate hydrophilic PAA blocks within star-like PS-*b*-PAA-*b*-PS triblock copolymers. The addition of reducer initiates the nucleation and growth of PS-capped Au NPs. In a typical procedure, star-like PS-*b*-PAA-*b*-PS (i.e., nanoreactor, 10 mg) was completely dissolved in a mixed solvent composed of DMF (9 mL) and BA (1 mL) at room temperature under stirring, followed by the addition of precursors ($HAuCl_4{\cdot}3H_2O$). For ensuring the maximum incorporation of precursors into the PAA compartment within the nanoreactors, 10-times (molar ratio) of precursors over acrylic acid (AA) units in PAA blocks were applied. It is notable that the mixture was stirred at room temperature under argon to thoroughly dissolve all the chemicals (except reducer) for a week. Subsequently, 10-times of reducers (ethanol) to precursors based on the molar ratio was added to the reaction system. The reaction was then performed at 60 °C under argon. After reacting for 10 h, the solution was centrifuged at 1000 rpm to remove the precipitates and purified by ultracentrifugation with nonpolar solvents (e.g., toluene) and precipitant (e.g., ethanol) several times to remove unreacted precursors and mixed solvent, yielding PS-capped hollow Au NPs.

Synthesis of PS-Capped Hollow Ag Nanoparticles. Another type of hollow noble metal NPs, that is, Ag NPs capped with PS, were also synthesized by employing star-like PS-*b*-PAA-*b*-PS triblock copolymers as nanoreactors. All experimental conditions and the formation mechanism of Ag NPs remained the same as those of PS-capped hollow Au NPs except that the precursors were changed to $AgNO_3$. Likewise, 10-times (molar ratio) of precursors over acrylic acid (AA) units in PAA blocks were added for the maximum incorporation of precursors into the PAA compartment within the nanoreactors. Similarly, to completely dissolve all the chemicals, the mixture solution (without reducer) was prestirred under argon at room temperature for a week. Subsequently, 10-times of ethanol as reducer to precursors based on the molar ratio was added into the reaction system. The reaction was then performed at 100 °C under argon. After reacting for 10 h, the same purification procedure as PS-capped hollow Au NPs was taken to obtain PS-capped hollow Ag NPs.

Encapsulation of Dyes. Because of the hollow interior and hairy polymer chains on the surface of NPs, a straightforward and viable route was developed to encapsulate RhB dye as a model guest molecule. Typically, polymer-capped hollow Au NPs $CHCl_3$ solution (0.5 mL, ∼1.4 nmol; hollow Au 2) was mixed with the RhB $CHCl_3$ solution (1.0 mL, 7 mg mL^{-1}). After stirring at room temperature for 24 h, methanol (5.0 mL) was added to the mixture. The dye-loaded NPs were obtained by centrifugation at 6500 rpm and washed with methanol (1.0 mL) several times until the absorbance at 550 nm of the supernatant in UV−vis spectrum was less than 0.01.

Dye Release from the Polymer-Capped Hollow NPs. To study the dye release behavior, we redispersed RhB-loaded NPs in $CHCl_3$ (1.0 mL). At predetermined times, methanol (5 mL) was added to the system followed by centrifugation at 6500 rpm. The supernatant was collected for UV−vis measurement. The amount of RhB molecules released from hollow NPs into solution was monitored by recording the absorbance at 550 nm of the supernatant at different times.

Characterizations. The number-average molecular weight (M_n) and polydispersity index (PDI) of prepared polymers were recorded by gel permeation chromatography (GPC) equipped with an LC-20AD HPLC pump and a refractive index detector (RID-10A, 120 V) at 35 °C. A series of monodisperse polystyrenes was used as the standard samples to calibrate GPC. THF was used as the eluent at a flow rate of 1.0 mL/min^{-1}. Proton nuclear magnetic resonance (^{1}H NMR) spectra were determined on a Varian VXR-300 spectroscope using $CDCl_3$ or d_7-DMF as solvent.

The size distribution and morphology of PS-capped hollow Au and Ag NPs were measured by transmission electron microscope (TEM) (JEOL 100; operated at 100 kV) and high-resolution transmission electron microscope (HRTEM, TECNAIG2 F30; operated at 300 kV). TEM samples were prepared by dropping a diluted solution containing hollow NPs onto a carbon-coated copper TEM grid (300 mesh) and dried at room temperature. For star-like PS-*b*-PAA-*b*-PS, the TEM grids were stained with uranyl acetate prior to the TEM imaging. Ten microliters of freshly made saturated uranyl acetate aqueous solution was dropped onto the TEM grid containing samples. After 5 min, the excess solution was carefully absorbed by filter paper, and the TEM grids were then dried at room temperature. The plasmonic properties of NPs were evaluated by UV−vis spectroscopy (Varian; UV−vis−NIR spectrophotometer, Cary 5000). Dynamic light scattering (DLS) data were attained using a laser light scattering spectrometer (Malvern Autosizer 4700) at 25 °C. Samples for AFM measurements were prepared via spin-coating the dilute solution onto the Si substrate and observed using AFM (XE-100, Park Systems) in air at a scan rate of 0.5 Hz at 25 °C. N_2 adsorption−desorption isotherms and specific surface area (based on Brunauer−Emmett−Teller (BET) method) were measured using a Micrometerics ASAP 2020 apparatus. The crystalline structures of hollow NPs were examined by X-ray diffraction (XRD, X'pert PRO, Netherlands).

Theoretical Calculation on Surface Plasmon Resonance of Hollow Nanoparticles. The general solution for scattering and absorption of a plane electromagnetic wave from a single metal NP was performed based on Maxwell equations

$$\nabla \times \boldsymbol{H} = \boldsymbol{J}_c + \frac{\partial \boldsymbol{D}}{\partial t} \tag{1}$$

$$\nabla \times \boldsymbol{E} = -\frac{\partial \boldsymbol{B}}{\partial t} \tag{2}$$

The constitutive relationships describing the macroscopic properties of medium can be given by

$$\boldsymbol{J}_c = \sigma \boldsymbol{E} \tag{3}$$

$$\boldsymbol{B} = \mu_0 \mu_r \boldsymbol{H} \tag{4}$$

$$\boldsymbol{D} = \varepsilon_0 \varepsilon_r \boldsymbol{E} \tag{5}$$

where $\boldsymbol{H}$ is the magnetic field intensity, $\boldsymbol{E}$ is the electric field intensity, $\boldsymbol{D}$ is the electric displacement, $\boldsymbol{B}$ is the magnetic flux density, and $\boldsymbol{J}_c$ is the conduction current density. The electromagnetic constants are the permeability of vacuum μ_0 and permittivity of vacuum ε_0. The response of a material to an electromagnetic wave is expressed through

DOI: 10.1021/jacs.7b04545
J. Am. Chem. Soc. 2017, 139, 12956−12967

physical parameters of material including the relative permeability μ_r, the relative permittivity ε_r, and the electric conductivity of medium σ.

By substituting eqs 1 and 4 into eq 2 and taking the curl of eq 2, the electric field intensity $\boldsymbol{E}$ satisfies the wave equation

$$\nabla \times \frac{1}{\mu_0 \mu_r} \nabla \times \boldsymbol{E} = -\frac{\partial}{\partial t}\left(\boldsymbol{J}_c + \frac{\partial \boldsymbol{D}}{\partial t}\right) \tag{6}$$

The relative permeability μ_r is set to $\mu_r = 1$ in the visible light region, which has been shown by experiment and theory.[62] The item $\boldsymbol{J}_c + \frac{\partial \boldsymbol{D}}{\partial t}$ on the right of eq 6 is defined as the total current density $\boldsymbol{J}$. For time harmonic field $\boldsymbol{E}(\boldsymbol{r},t) = \boldsymbol{E}_0(\boldsymbol{r})\exp(-i\omega t)$, the total current density $\boldsymbol{J}$ can thus be written as

$$\boldsymbol{J} = \boldsymbol{J}_c + \frac{\partial \boldsymbol{D}}{\partial t} = \left(i\frac{\sigma}{\omega} + \varepsilon_0 \varepsilon_r\right)\frac{\partial \boldsymbol{E}}{\partial t} \tag{7}$$

On the basis of electromagnetic theory, the total current density $\boldsymbol{J}$ can be expressed as $J = \varepsilon' \frac{\partial \boldsymbol{E}}{\partial t}$.[62] Thus, the dielectric constant ε' can be given as

$$\varepsilon' = \varepsilon_0\left(\varepsilon_r + i\frac{\sigma}{\omega\varepsilon_0}\right) \tag{8}$$

Therefore, for metals, the conductivity contributes to the imaginary part of ε'.

The macroscopic response of materials to an electromagnetic wave is reflected by their dielectric constant. The dielectric constant of metals is originated from the conduction electrons and all other electrons at deeper levels (i.e., core levels). For metals such as alkalis, ε' is mainly governed by transitions within the conduction band, whereas in noble metals such as Au and Ag, which constitute special monovalent metals, substantial contributions are from transitions not only within the conduction band but also from lower-lying bands into the conduction band.[63] We note that the measured dielectric constants of Au and Ag are used directly in our numerical calculation.[64]

Under experimental conditions, the rates at which energy from the incoming light is scattered and absorbed are of much interest. The sum of the absorbed energy from the incident wave in the integrated volume and the scattering energy of NP is defined as the extinction cross-section.[65] For the small sized NPs investigated in this work, the absorption dominated over the scattering by approximately 100 times. Therefore, the extinction cross-section is assumed to exclusively reflect the absorption. The absorption cross-section, $\delta_{abs}(\omega)$, of NPs is obtained by integrating the absorbed power density over the entire volume, V, such that

$$\delta_{abs}(\omega) = \frac{2}{c\varepsilon_0}\int_V [\sigma(\omega)\boldsymbol{E}\cdot\boldsymbol{E}^* - i\omega\boldsymbol{E}\cdot\boldsymbol{D}^*]\, dV \tag{9}$$

where the electric field intensity $\boldsymbol{E}$ and electric displacement $\boldsymbol{D}$ can be obtained by numerically solving eq 6. Numerical calculation was performed using COMSOL Multiphysics (COMSOL Inc., Burlington, MA). The design of the theoretical model was based on our TEM measurements on as-prepared NPs. Figure S10a depicts the schematic of the computational model. The incident electric field, $E_z = E_0\exp i(k,r - \omega t)$, used in the calculation propagates along the r axis with polarization in the z direction. Because of the spherical symmetry of the calculated model, when the perpendicular electric field of E_z, i.e. $E_r = E_0\exp i(k_z z - \omega t)$, was used as the incident field, the calculated result is the same. The surrounding medium of metal NPs is toluene whose optical parameters have been reported in the literature.[66] The computational domain was artificially truncated by the scattering boundary condition, which was placed sufficiently far from NP to minimize the effect of this artificial boundary.

■ ASSOCIATED CONTENT

Supporting Information

The Supporting Information is available free of charge on the ACS Publications website at DOI: 10.1021/jacs.7b04545.

Experimental details, ^{1}H NMR spectra, -COOH group schemes, TEM and AFM height images, nitrogen adsorption-desorption isotherms, UV−vis spectra, SRP simulation scheme, molecular weights and dimensions of copolymers, hydrodynamic diameters, simulated SPR peak positions and their dimensions, and simulated shell thickness dependences (PDF)

■ AUTHOR INFORMATION

Corresponding Authors

*msgzzhang@scut.edu.cn

*zhiqun.lin@mse.gatech.edu

ORCID

Xinchang Pang: 0000-0003-2445-5221

Zhiqun Lin: 0000-0003-3158-9340

Notes

The authors declare no competing financial interest.

■ ACKNOWLEDGMENTS

This work is supported by Air Force Office of Scientific Research (FA9550-16-1-0187), National Science Foundation (CMMI 1562075 and 1727313; DMR 1709420), and National Study Fund Committee (Project number: 2016-QT-049). Y.C. gratefully acknowledges the financial support from the SCUT Doctoral Student Short-Term Overseas Visiting Study Funding Project.

■ REFERENCES

(1) Jin, R.; Cao, Y.; Mirkin, C. A.; Kelly, K.; Schatz, G. C.; Zheng, J. *Science* **2001**, *294*, 1901.

(2) Zhou, J.; Pu, C.; Jiao, T.; Hou, X.; Peng, X. *J. Am. Chem. Soc.* **2016**, *138*, 6475.

(3) Sun, Y.; Xia, Y. *Science* **2002**, *298*, 2176.

(4) Jana, N. R.; Gearheart, L.; Murphy, C. J. *Adv. Mater.* **2001**, *13*, 1389.

(5) Pang, X.; He, Y.; Jung, J.; Lin, Z. *Science* **2016**, *353*, 1268.

(6) Huang, M. H.; Mao, S.; Feick, H.; Yan, H.; Wu, Y.; Kind, H.; Weber, E.; Russo, R.; Yang, P. *Science* **2001**, *292*, 1897.

(7) Hao, E.; Kelly, K. L.; Hupp, J. T.; Schatz, G. C. *J. Am. Chem. Soc.* **2002**, *124*, 15182.

(8) Newhouse, R. J.; Wang, H.; Hensel, J. K.; Wheeler, D. A.; Zou, S.; Zhang, J. Z. *J. Phys. Chem. Lett.* **2011**, *2*, 228.

(9) Gao, J.; Zhang, B.; Zhang, X.; Xu, B. *Angew. Chem., Int. Ed.* **2006**, *45*, 1220.

(10) Liu, H.; Qu, J.; Chen, Y.; Li, J.; Ye, F.; Lee, J. Y.; Yang, J. *J. Am. Chem. Soc.* **2012**, *134*, 11602.

(11) An, K.; Hyeon, T. *Nano Today* **2009**, *4*, 359.

(12) Kim, S.-W.; Kim, M.; Lee, W. Y.; Hyeon, T. *J. Am. Chem. Soc.* **2002**, *124*, 7642.

(13) Prodan, E.; Radloff, C.; Halas, N. J.; Nordlander, P. *Science* **2003**, *302*, 419.

(14) Caruso, F.; Caruso, R. A.; Möhwald, H. *Science* **1998**, *282*, 1111.

(15) Qi, L.; Li, J.; Ma, J. *Adv. Mater.* **2002**, *14*, 300.

(16) Peng, Q.; Dong, Y.; Li, Y. *Angew. Chem., Int. Ed.* **2003**, *42*, 3027.

(17) Kim, S. S.; Zhang, W.; Pinnavaia, T. J. *Science* **1998**, *282*, 1302.

(18) Sun, Y.; Xia, Y. *J. Am. Chem. Soc.* **2004**, *126*, 3892.

(19) Lu, X.; Tuan, H.-Y.; Chen, J.; Li, Z.-Y.; Korgel, B. A.; Xia, Y. *J. Am. Chem. Soc.* **2007**, *129*, 1733.

(20) Sun, Y.; Zuo, X.; Sankaranarayanan, S. K.; Peng, S.; Narayanan, B.; Kamath, G. *Science* **2017**, *356*, 303.

(21) Wang, W.; Dahl, M.; Yin, Y. *Chem. Mater.* **2013**, *25*, 1179.

(22) Yin, Y.; Rioux, R. M.; Erdonmez, C. K.; Hughes, S.; Somorjai, G. A.; Alivisatos, A. P. *Science* **2004**, *304*, 711.

(23) Zeng, H. C. *J. Mater. Chem.* **2006**, *16*, 649.

(24) Sun, Y.; Mayers, B.; Xia, Y. *Adv. Mater.* **2003**, *15*, 641.

(25) Zhang, Q.; Xie, J.; Lee, J. Y.; Zhang, J.; Boothroyd, C. *Small* **2008**, *4*, 1067.
(26) Yang, H. G.; Zeng, H. C. *J. Phys. Chem. B* **2004**, *108*, 3492.
(27) Boles, M. A.; Ling, D.; Hyeon, T.; Talapin, D. V. *Nat. Mater.* **2016**, *15*, 141.
(28) Hirsch, L. R.; Stafford, R. J.; Bankson, J.; Sershen, S. R.; Rivera, B.; Price, R.; Hazle, J. D.; Halas, N. J.; West, J. L. J. *Proc. Natl. Acad. Sci. U. S. A.* **2003**, *100*, 13549.
(29) Kam, N. W. S.; O'Connell, M.; Wisdom, J. A.; Dai, H. J. *Proc. Natl. Acad. Sci. U. S. A.* **2005**, *102*, 11600.
(30) He, Y.; Pang, X.; Jiang, B.; Feng, C.; Harn, Y. W.; Chen, Y.; Yoon, Y. J.; Pan, S.; Lu, C.-H.; Chang, Y. *Angew. Chem., Int. Ed.* **2017**, DOI: 10.1002/anie.201706182.
(31) Pang, X.; Zhao, L.; Akinc, M.; Kim, J. K.; Lin, Z. *Macromolecules* **2011**, *44*, 3746.
(32) Pang, X.; Zhao, L.; Han, W.; Xin, X.; Lin, Z. *Nat. Nanotechnol.* **2013**, *8*, 426.
(33) Chen, Y.; Yoon, Y.; Pang, X.; He, Y.; Jung, J.; Feng, C.; Zhang, G.; Lin, Z. *Small* **2016**, *12*, 6714.
(34) He, M.; Pang, X.; Liu, X.; Jiang, B.; He, Y.; Snaith, H.; Lin, Z. *Angew. Chem., Int. Ed.* **2016**, *55*, 4280.
(35) Xu, H.; Pang, X.; He, Y.; He, M.; Jung, J.; Xia, H.; Lin, Z. *Angew. Chem., Int. Ed.* **2015**, *54*, 4636.
(36) Jiang, B.; Pang, X.; Li, B.; Lin, Z. *J. Am. Chem. Soc.* **2015**, *137*, 11760.
(37) Matyjaszewski, K.; Tsarevsky, N. V. *Nat. Chem.* **2009**, *1*, 276.
(38) Feng, C.; Pang, X.; He, Y.; Li, B.; Lin, Z. *Chem. Mater.* **2014**, *26*, 6058.
(39) Feng, C.; Pang, X.; He, Y.; Chen, Y.; Zhang, G.; Lin, Z. *Polym. Chem.* **2015**, *6*, 5190.
(40) Koh, H.-D.; Park, S.; Russell, T. P. *ACS Nano* **2010**, *4*, 1124.
(41) Seo, E.; Kim, J.; Hong, Y.; Kim, Y. S.; Lee, D.; Kim, B.-S. *J. Phys. Chem. C* **2013**, *117*, 11686.
(42) Yang, D.; Pang, X.; He, Y.; Wang, Y.; Chen, G.; Wang, W.; Lin, Z. *Angew. Chem., Int. Ed.* **2015**, *54*, 12091.
(43) Ojea-Jiménez, I.; Romero, F. M.; Bastús, N. G.; Puntes, V. *J. Phys. Chem. C* **2010**, *114*, 1800.
(44) Aizawa, M.; Buriak, J. M. *J. Am. Chem. Soc.* **2005**, *127*, 8932.
(45) Liu, Y.; He, L.; Xu, C.; Han, M. *Chem. Commun.* **2009**, *0*, 6566.
(46) Li, B.; Han, W.; Jiang, B.; Lin, Z. *ACS Nano* **2014**, *8*, 2936.
(47) Möller, M.; Spatz, J. P.; Roescher, A. *Adv. Mater.* **1996**, *8*, 337.
(48) Ho, R.-M.; Lin, T.; Jhong, M.-R.; Chung, T.-M.; Ko, B.-T.; Chen, Y.-C. *Macromolecules* **2005**, *38*, 8607.
(49) Ben Moshe, A.; Markovich, G. *Chem. Mater.* **2011**, *23*, 1239.
(50) Sasidharan, M.; Senthil, C.; Kumari, V.; Bhaumik, A. *Chem. Commun.* **2015**, *51*, 733.
(51) Smoukov, S. K.; Bishop, K. J.; Kowalczyk, B.; Kalsin, A. M.; Grzybowski, B. A. *J. Am. Chem. Soc.* **2007**, *129*, 15623.
(52) Rycenga, M.; Wang, Z.; Gordon, E.; Cobley, C. M.; Schwartz, A. G.; Lo, C. S.; Xia, Y. *Angew. Chem., Int. Ed.* **2009**, *48*, 9924.
(53) Peng, S.; Sun, S. *Angew. Chem., Int. Ed.* **2007**, *46*, 4155.
(54) Penn, R. L.; Banfield, J. F. *Science* **1998**, *281*, 969.
(55) Kuroda, Y.; Watanabe, T.; Yoshikawa, Y.; Kumashiro, R.; Hamano, H.; Nagao, M. *Langmuir* **1997**, *13*, 3823.
(56) Rodriguez-Hernandez, J.; Chécot, F.; Gnanou, Y.; Lecommandoux, S. *Prog. Polym. Sci.* **2005**, *30*, 691.
(57) Daniel, M.-C.; Astruc, D. *Chem. Rev.* **2004**, *104*, 293.
(58) Lal, S.; Grady, N. K.; Kundu, J.; Levin, C. S.; Lassiter, J. B.; Halas, N. J. *Chem. Soc. Rev.* **2008**, *37*, 898.
(59) Wang, H.; Wu, Y.; Lassiter, B.; Nehl, C. L.; Hafner, J. H.; Nordlander, P.; Halas, N. J. *Proc. Natl. Acad. Sci. U. S. A.* **2006**, *103*, 10856.
(60) Hao, E.; Li, S.; Bailey, R. C.; Zou, S.; Schatz, G. C.; Hupp, J. T. *J. Phys. Chem. B* **2004**, *108*, 1224.
(61) Nagata, S.; Kokado, K.; Sada, K. *Chem. Commun.* **2015**, *51*, 8614.
(62) Drude, P. *The theory of optics*; Dover Publications: Dover, NY, 1959.
(63) Kreibig, U.; Vollmer, M. *Optical properties of metal clusters*; Springer-Verlag: Brilin Heidelberg, Germany, 1995; Vol. 25.
(64) Ordal, M.; Long, L.; Bell, R.; Bell, S.; Bell, R.; Alexander, R.; Ward, C. *Appl. Opt.* **1983**, *22*, 1099.
(65) Quinten, M. *Optical properties of nanoparticle systems: Mie and beyond*; Wiley-VCH Verlag & Co. KGaA: Weinheim, Germany, 2011.
(66) Samoc, A. *J. Appl. Phys.* **2003**, *94*, 6167.

DOI: 10.1021/jacs.7b04545
J. Am. Chem. Soc. 2017, 139, 12956−12967